JOURNAL OF GUIDANCE, CONTROL, AND DYNAMICS
Vol. , No. ,

Hybrid Attitude Control for Nano-Spacecraft: Reaction Wheel Failure and Singularity Handling

Ahmed Mahfouz* and Dmitry Pritykin†
Skolkovo Institute of Science and Technology, 121205, Moscow, Russia
and
James Biggs‡
Polytechnic University of Milan, 20158 Milan, Italy

https://doi.org/10.2514/1.G005525

This paper addresses the attitude control of nano-spacecraft with three reaction wheels and three magnetorquers in low Earth orbits, and develops algorithms to maintain control when any one of the reaction wheels completely fails. In the event of a reaction wheel failure, it is shown that the key challenge of maintaining accurate autonomous three-axis tracking is a problem of singularity avoidance in control allocation. In particular, control law singularities occur depending on the type of orbit, the environment, and the attitude, where the system is no longer controllable. Two algorithmic singularity avoidance techniques based on singularity prediction and artifici'al potential functions are proposed. In addition, an optimized reaction wheel configuration is proposed to enhance singularity avoidance capability. To illustrate the effectiveness of the singularity avoidance control laws, they are tested in simulations that include the effects of perturbing environmental torques, reaction wheel jitter, and actuator misalignment.

I. Introduction

NANO-SPACECRAFT (1–15 kg) offer cost-efficient access to space due to their relatively small time to launch, volume, and mass. One of the development goals of nano-spacecraft is to increase their application envelope to include, for example, accurate imaging or deep-space observation, which require precise three-axis stabilization and efficient slew maneuvers. Commercial-off-the-shelf (COTS) components for nano-spacecraft include actuators for attitude control, such as magnetorquers (MTQs) and reactions wheels (RWs). RWs are generally used for precise attitude control; however, over a mission lifetime, RWs are subject to wear and tear, jitter, and frictional forces, which can often lead to failure. In contrast, MTQs are highly reliable and are used for course sun pointing, detumbling, and momentum dumping; see, for example, [1–3]. In addition, combined with an appropriate aerodynamic design, MTQs have the potential to be used for nadir-pointing [4].

Nano-spacecraft RWs have a much higher risk of failure than those of large spacecraft [5]; therefore, either redundancy or fault-tolerant control algorithms are required. For nano-spacecraft with critical mass requirements, the possibility of developing fault-tolerant controls that alleviate the need for redundancy is highly desirable. In particular, a spacecraft is still controllable with two RWs and three MTQs, although with a decrease in efficiency and precision. Thus, this fault-tolerant control problem becomes one of minimizing the efficiency loss due to an RW failure. For example, single-axis pointing for a spacecraft with only two RWs is demonstrated in [6]. In theory, only two reaction wheels are required for three-axis stabilization and slew maneuvers [7,8]; however, the controllability of a spacecraft using only two RWs is dependent on the assumption of zero-total angular momentum, which is practically unrealistic to obtain and maintain without using additional actuators.

In the event of RW failure, it is sensible to consider coupling RWs and MTQs to perform tracking or slew maneuvers. Simultaneous use of MTQs and RWs has been proposed to save power and reduce RW torque requirements [9], whereas in this paper, their simultaneous use is considered in the event of an RW failure. In the first instance, a simple control allocation method is used; however, due to control allocation singularities, the system is shown to experience momentary attitude instabilities, or in the worst case, becomes uncontrollable [10]. A singularity is defined here as the system's state that belongs to the region at which the commanded control becomes infinite. Therefore, to maintain control using two RWs and MTQs, singularities must be avoided.

Such control law singularities have been analyzed for the REIMEI microsatellite [10], which is a bias-momentum spacecraft that uses three orthogonal MTQs and one momentum wheel for attitude control. In [10], Sakai et al. proposed a singularity-robust-inverse method for torque allocation to attenuate the effect of control law singularities; however, the generated torque does not match the required ones well in the vicinity of singular points.

Singularities have also been managed in the FUSE mission [11] when it lost two of its four RWs, and a hybrid control technique that used the remaining two RWs and the three MTQs had to be developed to perform the required slew maneuvers. In [11], ground-based predictions are suggested to be used to constrain science operations so that observations are scheduled at spacecraft orientations where sufficient torque can be generated to maintain fine pointing control during science exposures.

A two-reaction-wheel science control mode, which uses two RWs and four MTQs, is developed for the Hubble Space Telescope in [12]. To avoid singularities, the parameters of the command generator are specified for each individual maneuver. The computation of these parameters has to be carried out on the ground by planning and scheduling. It should be noted that the methods in [11,12] rely on ground-based predictions and are thus not suitable for completely autonomous spacecraft.

In this paper, two autonomous algorithms that do not require any ground-based calculations are proposed for the purpose of avoiding singularities. In addition, a reaction wheel arrangement is proposed in the design phase to enhance singularity avoidance. This modification is shown to minimize both the number of singularity encounters and the time the satellite spends in singular positions.

A tentative 3U CubeSat mission for ionospheric measurements that requires nadir-pointing in a near-polar circular orbit is presented to illustrate the effectiveness of the proposed techniques. The objective of the mission is to study the perturbations of the ionosphere in the polar areas. The mission is initially estimated to consist of a number of CubeSats that are equipped with langmuir probes as

Received 9 July 2020; revision received 16 September 2020; accepted for publication 17 September 2020; published online XX epubMonth XXXX.

*Master's Student, Space Center; ahmed.mahfouz@skoltech.ru.
†Senior Research Scientist, Space Center; d.pritykin@skoltech.ru.
‡Associate Professor, Department of Aerospace Science and Technology, Lombardy; jamesdouglas.biggs@polimi.it.

science instruments. The payload of the mission requires the least moment of inertia axis to point to the Earth, with an initial estimate of 3 deg allowable pointing error. Each CubeSat is assumed to initially contain three orthogonal reaction wheels and three orthogonal MTQs. Each set of actuators is aligned with the three principal moment of inertia axes. One of the spacecraft is assumed to experience complete failure of one of its RWs. Note that the problem of actuators' fault detection and isolation is out of the scope of this paper; however, it has been broadly investigated in the literature; see, for example, [13,14].

The paper is structured such that the basic mathematical model is presented in Sec. II. Section III contains a discussion of the first attempt to control the satellite using a quaternion feedback controller in conjunction with an inverse-dynamics allocation law. A satellite equipped with this control algorithm is shown to encounter singularities. Section IV presents two algorithmic singularity avoidance techniques. In addition, an optimized reaction wheel configuration is proposed to enhance the singularity avoidance capability of the spacecraft, and Sec. V presents the numerical simulations' results using such methods. Moreover, it discusses the potential of the proposed techniques to be generalized for different missions in different orbits.

II. Mathematical Model

A. Reference Frames

The following reference frames are used in the paper:

1) The Earth-centered inertial (ECI) reference frame $\mathcal{F}^i$, whose origin is at Earth's center and axes coincide with those of the J2000 frame.

2) The Earth-centered Earth-fixed (ECEF) reference frame $\mathcal{F}^f$, whose origin is at the Earth's center, z axis directed along the mean rotational axis of the Earth, x axis pointing to the Greenwich meridian, and y axis completes the right-handed system.

3) The orbital reference frame $\mathcal{F}^o$ with the origin at the center of mass of the satellite, z axis pointing away from the center of the Earth, y axis along the cross product of the satellite's center of mass position and velocity vectors, and x axis completing the frame according to the right-hand rule.

4) The body-fixed reference frame $\mathcal{F}^b$ with the origin at the satellite's center of mass. Its three axes coincide with the three principal axes of inertia of the satellite.

All vector transformations between reference frames are described by quaternions (see Appendix C).

B. Attitude Dynamics and Kinematics

The dynamic equations of motion for a spacecraft that has an RW module can be stated as

$$\begin{aligned} \mathbb{J}^b\dot{\boldsymbol{\omega}}^b &= -\boldsymbol{\omega}^b \times (\mathbb{J}^b\boldsymbol{\omega}^b + \mathbb{A}_w^b\boldsymbol{h}_w) + \boldsymbol{M}_{\text{ctrl}}^b + \boldsymbol{d}_{\text{tot}}^b, \\ \mathbb{A}_w^b\dot{\boldsymbol{h}}_w &= -\boldsymbol{M}_{\text{rw}}^b \end{aligned} \tag{1}$$

where $\mathbb{J}^b$ denotes the inertia tensor of the spacecraft, $\boldsymbol{\omega}^b = [\,\omega_x \quad \omega_y \quad \omega_z\,]^T$ is its angular velocity vector, $\mathbb{A}_w^b$ is the RW module's configuration matrix, $\boldsymbol{h}_w$ is the vector that contains the angular momentum of each RW in the module (see Appendix B.B), $\boldsymbol{M}_{\text{ctrl}}^b$ is the control torque provided by the actuators, $\boldsymbol{M}_{\text{rw}}^b$ is the torque generated by the RW module, and $\boldsymbol{d}_{\text{tot}}^b$ is the total disturbing torque acting on the spacecraft.

The total disturbing torque results from the environmental torques and the actuators' noise torques. It can be expressed as follows:

$$\boldsymbol{d}_{\text{tot}}^b = \boldsymbol{d}_{\text{act}}^b + \boldsymbol{d}_{\text{gg}}^b + \boldsymbol{d}_{\text{aer}}^b + \boldsymbol{d}_{\text{res}}^b + \boldsymbol{d}_{\text{srp}}^b \tag{2}$$

where $\boldsymbol{d}_{\text{act}}^b$ is the sum of actuators' disturbance torques, $\boldsymbol{d}_{\text{gg}}^b$ is the gravity-gradient torque, $\boldsymbol{d}_{\text{aer}}^b$ is the aerodynamic drag torque, $\boldsymbol{d}_{\text{res}}^b$ is the residual magnetization torque, and $\boldsymbol{d}_{\text{srp}}^b$ is the solar radiation pressure torque.

The kinematics of the spacecraft are described in unit quaternion form:

$$\dot{\mathfrak{q}}^{ib} = \frac{1}{2}\mathfrak{q}^{ib} \circ \boldsymbol{\omega}^b \tag{3}$$

Refer to Appendix C for the fundamentals of quaternion operations. In Appendix C, the mathematical model is extended to include environmental disturbance torques, as well as sensor, actuator, and system uncertainty models.

III. Attitude Control with an RW Failure

In this section, the case of complete failure of one RW is considered. After the failure of an RW is detected by the adopted fault detection algorithm, suitable control and torque allocation laws are triggered. Again, it is assumed that the initial system without failure consists of three reaction wheels and three MTQs aligned with the axes of the $\mathcal{F}^b$ frame.

A. Error-Quaternion Feedback Control

The ideal control torque $\boldsymbol{M}_{\text{ctrl}}^b = [M_x\ M_y\ M_z]^T$, which guarantees asymptotic stability of the system (provided that the system is not affected by noise), can be calculated by the following error-quaternion feedback control law [15]:

$$\boldsymbol{M}_{\text{ctrl}}^b = \boldsymbol{\omega}^b \times \left(\mathbb{J}^b\boldsymbol{\omega}^b + \mathbb{A}_w^b\boldsymbol{h}_w\right) - \mathbb{K}_d\boldsymbol{\omega}_e - q_{e,0}\mathbb{K}_p\boldsymbol{q}_e \tag{4}$$

where $\mathbb{K}_d$ and $\mathbb{K}_p$ are 3×3 gain matrices, $\mathfrak{q}_e = [\,q_{e,0} \quad \boldsymbol{q}_e\,]^T$ is the error unit quaternion, and $\boldsymbol{\omega}_e$ is the angular velocity error vector. The error quaternion is defined as follows:

$$\mathfrak{q}_e = \tilde{\mathfrak{q}}_d \circ \mathfrak{q}^{ib} \tag{5}$$

The error angular velocity is defined as follows:

$$\boldsymbol{\omega}_e = \boldsymbol{\omega}^b - \tilde{\mathfrak{q}}_e \circ \boldsymbol{\omega}_d \circ \mathfrak{q}_e \tag{6}$$

where $\mathfrak{q}_d$ and $\boldsymbol{\omega}_d$ are the desired quaternion and angular velocity, which have to satisfy the kinematics equation (3). Refer to Appendix B.B for the definitions of $\mathbb{A}_w^b$ and $\boldsymbol{h}_w$. Note that in Eq. (4), $\mathbb{A}_w^b = \mathbb{I}_{3\times3}$ for the initial configuration that has three reaction wheels aligned with the axes of the $\mathcal{F}^b$ frame. The control law (4) can be generally used for slew maneuvers or tracking of slowly rotating frames.

B. Torque Allocation

In the event of reaction wheel failure, the controller (4) can be used for tracking and slew motions using two RWs and one MTQ. Combining Eqs. (B3) and (B12), the control torque can be expressed in terms of actuators' parameters as follows:

$$\boldsymbol{M}_{\text{ctrl}}^b = -\mathbb{A}_w^b\dot{\boldsymbol{h}}_w + \boldsymbol{m}^b \times \boldsymbol{B}^b \tag{7}$$

where $-\mathbb{A}_w^b\dot{\boldsymbol{h}}_w = [u_x\ u_y\ u_z]^T$ is the control torque produced by the RW module, $\boldsymbol{m}^b = [m_x\ m_y\ m_z]^T$ is the magnetic dipole moment vector produced by the MTQ set, and $\boldsymbol{B}^b = [B_x\ B_y\ B_z]^T$ is the true local magnetic field vector.

Allocating the control torque (4) to the available actuators can be done by solving Eq. (7) for $-\mathbb{A}_w^b\dot{\boldsymbol{h}}_w$ and $\boldsymbol{m}^b$ according to which one of the RWs has failed.

Let $\nu \in \{1, 2, 3\}$ be the index of the failed reaction wheel and $\mathcal{S} = \{1, 2, 3\} \setminus \{\nu\}$, and the solution to Eq. (7) can be written as follows:

$$
\begin{aligned}
k &= \arg\min_{i\in\mathcal{S}}(|B_i|),\\
\lambda_i &= \mathrm{Sat}\left(\frac{M_\nu}{B_i}, m_{\max}\right),\\
u_i &= (1-\delta_{i\nu})M_i + |\varepsilon_{i\nu k}|B_\nu\lambda_i,\\
m_j &= \delta_{jk}\sum_i(\varepsilon_{\nu ji}\lambda_i)
\end{aligned}
\tag{8}
$$

where $i, j \in \{1, 2, 3\}$, ε_{ijk} is the Levi–Civita symbol, δ_{ij} is the Kronecker delta, $\mathrm{Sat}(v, \alpha_v)$ is a saturation function illustrated by Eq. (B5), and $m_{\max}$ is the maximum dipole moment the MTQ can generate.

As the true geomagnetic field vector $\boldsymbol{B}^b$ is not known, the measured magnetic field $\boldsymbol{B}^b_{\mathrm{meas}}$ (B16) can be used instead to compute the values of u_i and m_j in Eq. (8).

Equation (8) is a control allocation rule that assigns the torque duties to each onboard actuator, depending on actuator failure situation. An example of its final form for the case of losing the reaction wheel in the z direction and compensating for this loss with the MTQ in the x direction is given in the following equation:

$$
\begin{bmatrix} u_x \\ u_y \\ m_x \end{bmatrix} = \begin{bmatrix} 1 & 0 & 0 \\ 0 & 1 & B_z \\ 0 & 0 & 1 \end{bmatrix} \begin{bmatrix} M_x \\ M_y \\ \lambda_y \end{bmatrix} \tag{9}
$$

Note that the torque allocation law (8) uses only one MTQ at a time, which makes it prone to fast switching between the MTQs at some specific points. This can be ruled out by introducing a torque allocation law that uses multiple MTQs simultaneously. Sharing the control effort across MTQs could reduce saturation; however, it is potentially less power efficient, yet this comparison is beyond the scope of this paper. Throughout the paper, the torque allocation law (8) is used; however, the potential to use other torque allocation laws that do not restrict themselves to using one MTQ at a time is an interesting venue for future research.

C. Mission Parameters

In this section, values for the parameters of the adopted mission are stated in detail. The values specified here are used in all subsequent simulations.

The mission is an Earth-pointing mission, which requires the $\mathcal{F}^b$ frame to be aligned with the $\mathcal{F}^o$ frame with an allowable pointing error of 3 deg. The satellite is a 3U CubeSat that has a mass of 3 kg and dimensions of 10 cm, 10 cm, and 34 cm. The estimated moment of inertia matrix is set to $\mathbb{J}^b = \mathrm{diag}(0.0309, 0.0319, 0.0051)\ \mathrm{kg}\cdot\mathrm{m}^2$. The satellite is inserted into a circular near-polar orbit at an altitude of 450 km and an inclination of 87 deg.

The satellite is assumed to have three identical RWs and three identical MTQs, each set aligned with the principal moment of inertia axes. The actuators of this mission are selected from the COTS hardware. The GOMspace NanoTorque GSW-600 reaction wheel module and the Hyperion Technologies MTQ200.20 magnetic rods are assumed to be used in this mission. Each of the RWs in the chosen module has a moment of inertia of $3\cdot10^{-5}\ \mathrm{kg}\cdot\mathrm{m}^2$, maximum wheel torque $\dot{h}_{\max} = 2\ \mathrm{mN}\cdot\mathrm{m}$, and maximum wheel angular momentum $h_{\max} = 19\ \mathrm{mN}\cdot\mathrm{m}\cdot\mathrm{s}$. The maximum magnetic dipole moment of the MTQ200.20 is $m_{\max} = 1\ \mathrm{A}\cdot\mathrm{m}^2$.

Levels of disturbances that act upon the system are summarized in Table 1.

The initial conditions for each simulation are random, and each component of the initial angular velocity vector is bounded by 5 deg/s. The desired attitude is $\mathfrak{q}_d = \mathfrak{q}^{io}$, which is to align the $\mathcal{F}^b$ frame with the $\mathcal{F}^o$ frame (i.e., Earth pointing). To meet the kinematics constraint, the desired angular velocity shall be $\boldsymbol{\omega}_d = \boldsymbol{\omega}^o_{o/i} = [0 \quad \omega_0 \quad 0]^T$, where ω_0 is the mean motion of the spacecraft in orbit.

Table 1 Levels of disturbances

	Symbol	Value	Unit	Reference
Environmental torques:				Appendix B.A
Gravity gradient	$\|\boldsymbol{d}^b_{\mathrm{gg}}\|$	$5\cdot10^{-8}$	$\mathrm{N}\cdot\mathrm{m}$	
Aerodynamic drag	$\|\boldsymbol{d}^b_{\mathrm{aer}}\|$	10^{-7}	$\mathrm{N}\cdot\mathrm{m}$	
Solar radiation pressure	$\|\boldsymbol{d}^b_{\mathrm{srp}}\|$	$1.5\cdot10^{-9}$	$\mathrm{N}\cdot\mathrm{m}$	
Residual magnetization	$\|\boldsymbol{d}^b_{\mathrm{re}}\|$	$4\cdot10^{-7}$	$\mathrm{N}\cdot\mathrm{m}$	
Reaction wheels:				Appendix B.B
Static imbalance	S_i	$5\cdot10^{-11}$	$\mathrm{kg}\cdot\mathrm{m}$	
Dynamic imbalance	D_i	10^{-11}	$\mathrm{kg}\cdot\mathrm{m}^2$	
Misalignment angle	θ_{mis}	1	deg	
Magnetorquers:				Appendix B.B
Magnetorquer noise	$3\sigma_m$	0.01	$\mathrm{A}\cdot\mathrm{m}^2$	
Determination errors:				Appendix B.C
$\boldsymbol{\omega}^b$ error	$3\sigma_\omega$	0.025	deg/s	
$\mathfrak{q}^{ib}$ angle error	$3\sigma_q$	0.5	Deg	
Magnetometer bias	μ_B	50	nT	
Magnetometer deviation	$3\sigma_B$	100	nT	
Inertia uncertainties:				Appendix B.D
Inertia moments	$\Delta\mathbb{J}$	$10\%\mathbb{J}$		
Axes misalignment	θ_J	1	deg	

D. Numerical Simulation Results

To demonstrate the capabilities of the quaternion feedback controller (4), three cases are considered, case X is when the RW aligned with the x axis fails ($\nu = 1$), case Y is when the RW aligned with the y axis fails ($\nu = 2$), and case Z is when the RW aligned with the z axis fails ($\nu = 3$). The controller gain matrices are tuned by trial and error for the mission parameters in Sec. III.C as in the following equation:

$$
\begin{aligned}
\mathbb{K}_p &= 5\cdot10^{-3}\mathbb{K},\\
\mathbb{K}_d &= 10^{-2}\mathbb{K}
\end{aligned}
\tag{10}
$$

where the $\mathbb{K}$ is defined in Table 2 for each of the cases.

One way to assess the performance of a certain attitude controller is to monitor the angle of the error quaternion [defined in Eq. (5)]. Typical responses of cases X, Y, and Z are shown in Fig. 1.

From Fig. 1, it is clear that the system is unstable under the implied constraints and noises when it has its wheel-less axis in the z direction of the $\mathcal{F}^b$ frame. On investigating the situation, it has been concluded that the system experiences what is referred to as singularities, which drive the satellite away from its equilibrium. These singularities take place when the MTQs are not able to realize the control requirements for a long period of time. (A detailed discussion of this phenomenon is presented in Sec. III.E.)

Equation (B12) shows that MTQs cannot physically generate torque in the direction of the local magnetic field; that is why when the $\boldsymbol{B}^b$ is nearly aligned with the ν axis, the MTQs cease to provide the necessary control torque, and when this situation lasts for a sufficiently long period, the system reaches an unstable state. In Fig. 2, the projection of the unit vector $\hat{\boldsymbol{B}}^o$ (using the IGRF12 model) on the ν axis is plotted for the three possible values of ν against the argument of latitude of the satellite (u) for the first orbital revolution to illustrate why controller (4) works fine for cases X and Y, whereas it does not work for case Z. Note that $\hat{\boldsymbol{B}}^o$ is identical to $\hat{\boldsymbol{B}}^b$ when the system reaches the steady state for the adopted case study that requires Earth pointing.

Table 2 Controller gain matrices

	Case X	Case Y	Case Z
$\mathbb{K}$	diag (0.05, 1, 1)	diag (1, 0.05, 1)	diag (1, 1, 0.05)

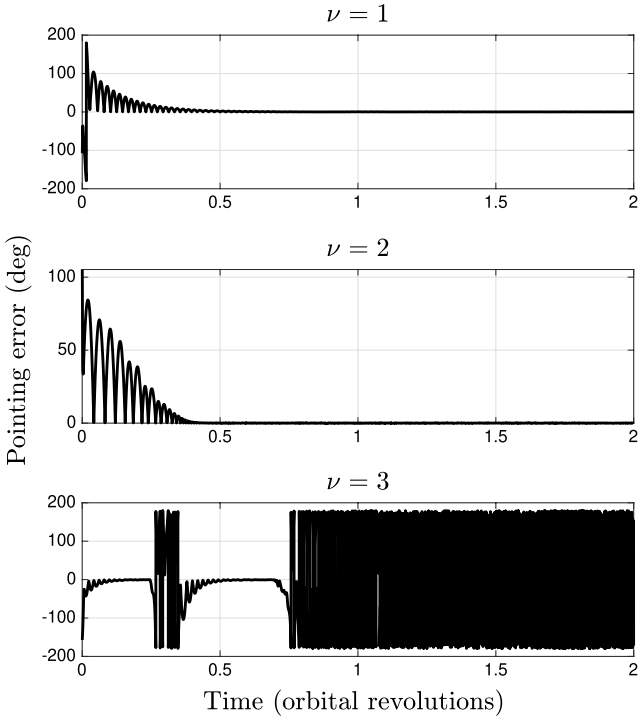

Fig. 1 Pointing error for cases X, Y, and Z.

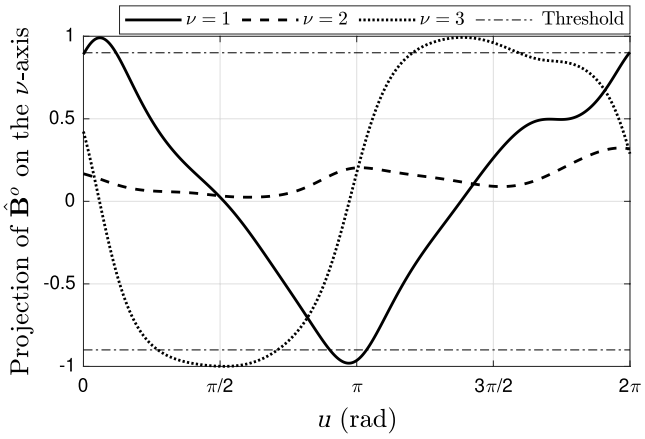

Fig. 2 Singular regions for cases X, Y, and Z.

A singularity threshold is introduced for the unit geomagnetic field vector projection onto the ν axis. It is a constant value to delineate a near-singularity zone such that a system that stays over the threshold eventually becomes uncontrollable. For the case study defined in Sec. III.C, this threshold is empirically determined to be 0.9. For case X ($\nu = 1$), the projection of the unit magnetic field vector on the ν axis goes over the threshold for about 24 deg arc measure every half orbit. Nonetheless, the controller (4) appears to stabilize the system as seen in Fig. 1. There is no wonder why case Y ($\nu = 2$) is stabilized by controller (4), as the magnetic field projection on the wheel-less axis does not reach the threshold at all. For case Z ($\nu = 3$), however, the projection of $\hat{\boldsymbol{B}}^o$ on the ν axis reaches beyond the threshold for almost 96 deg arc measure each half a revolution; that is why the attitude of the spacecraft comes to an uncontrollable state for this case (see Fig. 1).

E. Singularity Illustration

In this section, singularities are illustrated mathematically and graphically. It is important to have a graphical understanding of how singularities affect the system because one of the singularity avoidance approaches that we propose in Sec. IV significantly relies on the geometry.

Singularities can be seen mathematically in the control allocation law (8), where B_i can have values close to zero. When $B_i \approx 0$, m_j is forced to the saturation limit that cannot meet the controller requirements, which in turn leads to loss of stability. If the wheel-less axis is the ν axis, then, according to Eq. (8), $k \in \mathcal{S}$, which suggests two possible values for k. The choice of k determines which MTQ to be used to compensate for the RW loss in the ν axis. With this in mind, k alternates between its two possible values so that the magnetic field projection on the axis of the used MTQ is minimized, hoping that it will be maximized on the unchosen k axis. It is problematic, however, when the projection of $\boldsymbol{B}^b$ is close to zero in the two available k axes, namely, when the local geomagnetic field vector $\boldsymbol{B}^b$ coincides with the ν axis. That is when a MTQ is required to provide more torque than it physically can.

In general, singularities exist when the magnetic field vector is parallel to the wheel-less axis (the ν axis). Consider, for example, the equatorial orbit (Orbit-A in Fig. 3), and assume, for simplicity, that the geomagnetic field is a dipole with poles that coincide with the geographic ones. After the spacecraft reaches the desired nadir-pointing attitude, the local magnetic field vector is almost always parallel to the y axis of the spacecraft's $\mathcal{F}^b$ frame. The satellite will not face any singularities if the ν axis lies in the equatorial plane; however, almost all the points along the orbit will be singular if the ν axis is normal to the orbital plane. The same generalization can be applied for highly inclined orbits (Orbit-B in Fig. 3); the geomagnetic field vector becomes almost parallel to the z axis of the $\mathcal{F}^b$ frame when the satellite is close to the poles, whereas it is nearly aligned to the x axis of the $\mathcal{F}^b$ frame nearby the equator. However, it does not become parallel to the y axis in any of the points along the orbit (see, e.g., Fig. 2). The question of whether the system will lose stability in this case is a question of how long the $\boldsymbol{B}^b$ vector will be nearly aligned with the ν axis.

Singularities are operative in the case of hybrid control using RWs and MTQs [11]. The gyroscopic torque, generated by the spinning reaction wheels and the slowly rotating spacecraft, is particularly effective in the axis that is not actuated by an RW because; first, it is not perfectly compensated for by the controller (4) due to determination errors and uncertainties, and second, the MTQ cannot compensate for it during singularities. This gyroscopic torque increases the rotational velocity of the spacecraft in the wheel-less axis, which in turn makes it hard for the spacecraft to recover from a singularity. Singularities do not have as much effect in full magnetic control systems as seen in the simulations in [16,17].

To sum up, the existence of singularities depends on mission requirements (Earth pointing, Sun pointing, etc.), the orbit (the

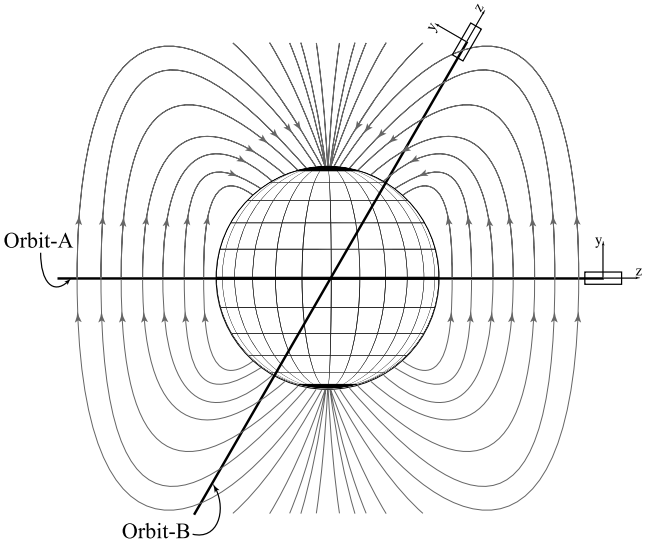

Fig. 3 Singularity illustration.

direction of the magnetic field vector), and the axis on which an RW is missing.

IV. Singularity Avoidance

In [11], Roberts et al. have analyzed the problem of not being able to achieve the control requirements at some portions of the orbit by the MTQs when only two RWs remain intact (what is referred to as a singularity here). They suggested to use ground-based predictions and constrain science operations so that observations are scheduled at spacecraft orientations where sufficient torque can be generated to maintain fine pointing control during science exposures.

In this section, three singularity avoidance techniques are proposed to autonomously evade singularities. These techniques do not require ground-based calculations or planning, in contrast to what has been proposed in [11,12]. The first technique proposes a controller with an artificial potential function (APF)–based controller, whereas the second relies on predicting the occurrence of singularities ahead of time using the onboard geomagnetic field model. If a singularity is predicted, the APF-based controller is triggered until the section of the orbit that contains singular points is over. The third technique proposes a change in the arrangement of the RW module during the design phase to minimize the probability of encountering singularities.

A. Artificial Potential Function-Based Controller

In Sec. III, the Lyapunov-based controller (4) is used to manipulate the attitude of the spacecraft; however, it does not guarantee the stability of the system when only two RWs are available due to the existence of singularities. A common way to avoid undesired states of a system (e.g., singular states) is to add an artificial potential term to the Lyapunov function [18,19]. A modified Lyapunov function with an additional artificial potential term is proposed in this section to avoid orientations that may cause singularities in orbit. The proposed potential function is expressed as follows:

$$V = \frac{1}{2}\boldsymbol{\omega}_e^T \mathbb{K}_p^{-1}\mathbb{J}^b\boldsymbol{\omega}_e + \left(1 - q_{e,0}^2\right) + \Lambda_3,$$
$$\Lambda_3 = \frac{1}{2}\alpha\exp\left[-\gamma\left(B_x^2 + B_y^2\right)\right] \tag{11}$$

where B_x and B_y are the x and y components of the local magnetic field vector $\boldsymbol{B}^b$, α and γ are tuning parameters, and $\mathbb{K}_p$ is a positive definite 3×3 gain matrix that insures that $(\mathbb{K}_p^{-1}\mathbb{J}^b)$ is symmetric.

It is important to note that the potential function (11) is proposed only for the case of losing an RW in the z direction of the $\mathcal{F}^b$ frame ($\nu = 3$), which is the extreme situation for the considered case study (see Fig. 1). It is possible, however, to generalize Eq. (11) when the spacecraft has its wheel-less axis in any direction ν, by changing the value of Λ according to the specific situation as follows:

$$\Lambda_\nu = \frac{1}{2}\alpha\exp\left[-\gamma\sum_i B_i^2\right], \qquad i \in \mathcal{S} \tag{12}$$

Taking the time derivative for both sides of Eq. (11) yields

$$\dot{V} = \boldsymbol{\omega}_e^T\mathbb{K}_p^{-1}\mathbb{J}^b\dot{\boldsymbol{\omega}}_e + (-2q_{e,0}\dot{q}_{e,0}) - \underbrace{\alpha\gamma\exp[-\gamma(B_x^2+B_y^2)]}_{\psi}\left(B_xB_x + B_yB_y\right) \tag{13}$$

The kinematic model of the error signals (i.e., $\boldsymbol{\omega}_e$ and $\mathfrak{q}_e$) is discussed in detail in Appendix B.E. Equations (B24) and (B28) can be rewritten as follows:

$$\dot{q}_{e,0} = -\frac{1}{2}\boldsymbol{\omega}_e^T\boldsymbol{q}_e \tag{14}$$

$$\dot{\boldsymbol{\omega}}_e = (\mathbb{J}^b)^{-1}\left\{-\boldsymbol{\omega}^b\times(\mathbb{J}^b\boldsymbol{\omega}^b + \mathbb{A}_w^b\boldsymbol{h}_w) + \boldsymbol{M}_{\text{ctrl}}^b + \mathbb{J}^b\left[\boldsymbol{\omega}_e\times(\tilde{\mathfrak{q}}_e\circ\boldsymbol{\omega}_d\circ\mathfrak{q}_e) - \tilde{\mathfrak{q}}_e\circ\dot{\boldsymbol{\omega}}_d\circ\mathfrak{q}_e\right]\right\} \tag{15}$$

The time derivative of the magnetic field vector can be calculated using the transport theorem as follows:

$$\dot{\boldsymbol{B}}^b = \dot{\boldsymbol{B}}^b|_b = \dot{\boldsymbol{B}}^b|_i - \boldsymbol{\omega}^b\times\boldsymbol{B}^b \tag{16}$$

where $\dot{\boldsymbol{v}}|_x$ denotes the rate of change of the vector $\boldsymbol{v}$ as seen by an observer attached to the $\mathcal{F}^x$ frame. For a detailed expansion of Eq. (16), refer to Appendix C.

Substituting from Eqs. (15), (14), and (C8) into Eq. (13), and assuming that $\boldsymbol{\omega}^b \approx \boldsymbol{\omega}_e$ in Eq. (C8) (which is true for missions that require tracking of a slowly evolving rotating frame), yields

$$\dot{V} = \boldsymbol{\omega}_e^T\{q_{e,0}\boldsymbol{q}_e + \psi\boldsymbol{p} + \mathbb{K}_p^{-1}\{-\boldsymbol{\omega}^b\times(\mathbb{J}^b\boldsymbol{\omega}^b + \mathbb{A}_w^b\boldsymbol{h}_w) + \boldsymbol{M}_{\text{ctrl}}^b + \mathbb{J}^b[\boldsymbol{\omega}_e\times(\tilde{\mathfrak{q}}_e\circ\boldsymbol{\omega}_d\circ\mathfrak{q}_e) - \tilde{\mathfrak{q}}_e\circ\dot{\boldsymbol{\omega}}_d\circ\mathfrak{q}_e]\}\} \tag{17}$$

where the vector $\boldsymbol{p}$ is defined as

$$\boldsymbol{p} = \begin{bmatrix} -B_yB_z \\ B_x[B_z + 3B_0\sin(\epsilon)\sin(u)] \\ 0 \end{bmatrix} \tag{18}$$

where $B_0 = \mu_e/\|\boldsymbol{r}\|$; $\mu_e = 7.812\cdot 10^{15}\ \text{T}\cdot\text{m}^3$; $\boldsymbol{r}$ is the position vector of the spacecraft's center of mass, expressed in any reference frame; u is the argument of latitude at the satellite position; and ϵ is the inclination of the orbital plane.

Note that in Eq. (17), $\mathbb{A}_w^b \neq \mathbb{I}_{3\times 3}$ as in the three orthogonal RWs case. It is rather a 3×2 configuration matrix that describes the directions of the angular momentum vectors of the two operational RWs. $\boldsymbol{h}_w$ in this case is a 2×1 vector.

One way to ensure that $\dot{V}$ is negative definite is using the following control law:

$$\boldsymbol{M}_{\text{ctrl}}^b = \boldsymbol{\omega}^b\times(\mathbb{J}^b\boldsymbol{\omega}^b + \mathbb{A}_w^b\boldsymbol{h}_w) - \mathbb{K}_p(q_{e,0}\boldsymbol{q}_e + \psi\boldsymbol{p}) - \mathbb{K}_d\boldsymbol{\omega}_e - \mathbb{J}^b[\boldsymbol{\omega}_e\times(\tilde{\mathfrak{q}}_e\circ\boldsymbol{\omega}_d\circ\mathfrak{q}_e) - \tilde{\mathfrak{q}}_e\circ\dot{\boldsymbol{\omega}}_d\circ\mathfrak{q}_e] \tag{19}$$

Controller (19) is more complicated than the simple quaternion feedback controller (4). For tracking of a slowly evolving rotating frame, the last two terms in Eq. (19) can be omitted for being relatively small in comparison to the other terms. For missions that require nadir-pointing in circular orbits, $\dot{\boldsymbol{\omega}}_d$ is strictly $\boldsymbol{0}$. The final form of the APF-based control law, which has to be used for an Earth-pointing mission, is presented as follows:

$$\boldsymbol{M}_{\text{ctrl}}^b = \boldsymbol{\omega}^b\times(\mathbb{J}^b\boldsymbol{\omega}^b + \mathbb{A}_w^b\boldsymbol{h}_w) - \mathbb{K}_p(q_{e,0}\boldsymbol{q}_e + \psi\boldsymbol{p}) - \mathbb{K}_d\boldsymbol{\omega}_e \tag{20}$$

As far as the computational resources are concerned, controller (20) is not computationally expensive. It differs from the quaternion-feedback controller (4) in computing the two simple expressions ψ and $\boldsymbol{p}$ for each control cycle.

As will be shown, the numerical simulations reveal that the APF-based controller (20) performs well, yet the performance is degraded in comparison to case X and case Y in Fig. 1. A satellite in a low Earth orbit is equipped with a geomagnetic field model, which can be made use of to predict whether the spacecraft will face a singularity within a preset prediction horizon, and hence trigger the APF-based controller only for the singular points on the orbit. The next section proposes using the APF-based controller only when a singularity is predicted.

B. APF-Based Controller with Singularity Prediction

As discussed in Sec. III.E, singularities arise from having the local magnetic field vector $\boldsymbol{B}^b$ aligned with the wheel-less axis, and when this alignment is kept for a long time, the control authority can be lost. The vector $\boldsymbol{B}^b$ is basically the geomagnetic field vector in the $\mathcal{F}^i$ frame only rotated to the $\mathcal{F}^b$ frame, $\boldsymbol{B}^b = \tilde{\mathfrak{q}}^{ib}\circ\boldsymbol{B}^i\circ\mathfrak{q}^{ib}$. Indeed, it is impossible to control the local magnetic field vector $\boldsymbol{B}^i$. It is possible, however, to change the attitude of the spacecraft before it encounters

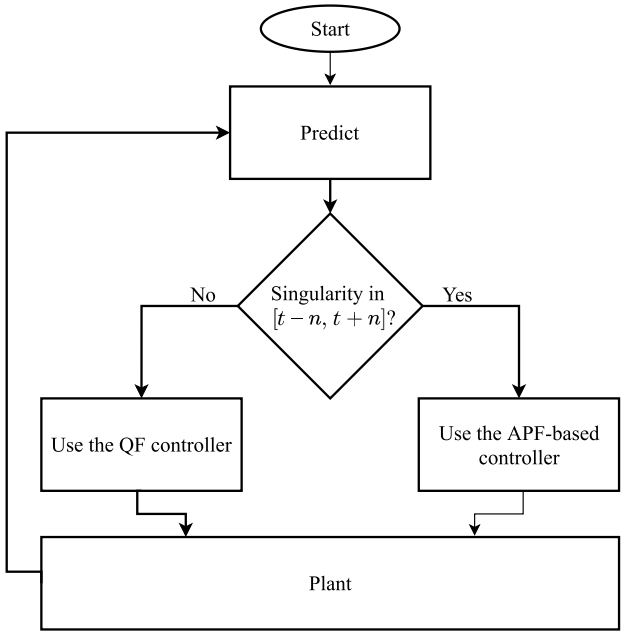

Fig. 4 Flowchart of the singularity prediction algorithm.

a singularity, which is essentially what the APF-based controller (20) does.

In the normal operation, the system is controlled by the quaternion feedback controller (4), while propagating the magnetic field vector ahead of time to predict singularities. If a singularity is predicted to happen n seconds in the future. The APF-based controller (20) is triggered n seconds before the first singular point, and remains on until n seconds after the last singular point. This algorithm is illustrated by the flowchart in Fig. 4. In this technique, two different controllers are used according to whether a singularity is predicted. For simplicity, these two controllers are referred to as the quaternion feedback controller (4) and the APF-based controller (20).

In Fig. 4, the prediction block is executed by predicting $\mathfrak{q}^{io}$ and $\boldsymbol{B}^i$, hence predicting $\boldsymbol{B}^b$, n steps ahead of time. It is assumed that the system follows any attitude it is ordered to follow, such that the desired quaternion for the nadir-pointing case study, $\mathfrak{q}^{io}$, can be considered equal to $\mathfrak{q}^{ib}$. Singularities are identified if the projection of the predicted unit vector $\hat{\boldsymbol{B}}^b$ on the wheel-less axis reaches the predefined threshold B_{th}.

As for the computational burden, the algorithm does not differ much from the APF-based controller (20). It varies from Eq. (20) only in running an additional iteration of the SGP4 propagator and another additional iteration of the magnetic field model. Besides, the computed results can be used in future control cycles if the memory allows. The algorithm can be implemented in a more sophisticated way at the expense of computational complexity if the APF controller is triggered when two conditions are satisfied: firstly when the projection of $\hat{\boldsymbol{B}}^b$ on the ν axis is predicted to be more than B_{th} within n seconds, and secondly when the model anticipates this projection to last above the projection threshold for more than an arc measure threshold u_{th}. It is known that the system in Sec. III.C handles singular points quite well when they successively last for 24 deg of the orbit as concluded by Figs. 1 and 2. For instance, this value can be set as the arc measure threshold for the simulated system.

C. Optimized RW Configuration

It is shown in Sec. V that after the loss of an RW, the major problem with maintaining the control quality with the use of the proposed algorithms occurs when passing through the turbulence zones near singular points, which leads to degradation of pointing accuracy. It stands to reason that the key to preserving the control quality is in avoiding such turbulence zones whenever possible. The problem of singularities can thus be addressed by choosing the RWs arrangement so as to minimize the number and duration of encounters with singularities. Since singularities are defined in terms of the geomagnetic field projection onto the axis of the lost RW, it is proposed here to install the RW assembly into a spacecraft taking into account the nominal attitude and orbit specifications in order to keep the geomagnetic field projection onto all RW axes below threshold throughout the mission lifetime.

In this section, a way to find an optimized arrangement of RWs is introduced. The resulting configuration from the proposed method is optimal from the point of view of singularities avoidance, as it minimizes the number of singular points the defined mission can encounter throughout its life time, and hence minimizes the time the spacecraft spans over these singular points.

An optimization problem is synthesized to find the optimized rotation of the RW assembly. The optimization aims to minimize the maximum projection of the geomagnetic field unit vector on the orthogonal RW axes at the critical point in the orbit. The critical point is the location of the satellite at which the maximum projection of $\hat{\boldsymbol{b}}^b$ along the RW axes reaches its maximum value.

Assuming that three RWs were initially aligned with the principal moment of inertia axes, the configuration matrix in this case is $\mathbb{A}_w^b = \mathbb{I}_{3\times 3}$. This arrangement can be changed for a new one by rotating each column vector in $\mathbb{A}_w^b$ by the direct cosine matrix $\mathbb{R}_w(\phi, \theta, \psi) = [\,\hat{\boldsymbol{R}}_1 \quad \hat{\boldsymbol{R}}_2 \quad \hat{\boldsymbol{R}}_3\,]$, which results from transforming the three Euler angles ϕ, θ, ψ (with order XYZ, for example) to a DCM. The new configuration matrix in this case is $\mathbb{A}_w^b = \mathbb{R}_w$.

The cost function can then be written as follows:

$$J(\phi, \theta, \psi) = \max_{u,\Omega^f}\Big[\max_i \big|\langle \hat{\boldsymbol{B}}^b, \boldsymbol{R}_i\rangle\big|\Big] \tag{21}$$

where $\langle , \rangle$ is the dot product operator, u is the argument of latitude, and Ω^f is the longitude of the ascending node (LAN). For an orbit with fixed semimajor axis, eccentricity, inclination, and argument of perigee, the possible combinations of $u \in [0, 2\pi)$ and $\Omega^f \in [0, 2\pi)$ cover all the possible positions of the satellite around the globe in this orbit.

The optimization problem is stated as follows:

$$\begin{aligned} &\text{Find} \quad \arg\min_{\phi,\theta,\psi}[J(\phi, \theta, \psi)], \\ &\text{Under constraints} \quad 0 \le \phi, \theta, \psi \le 2\pi \end{aligned} \tag{22}$$

V. Results and Discussion

In this section, the results of the numerical simulations for the mission in Sec. III.C using the proposed singularity avoidance techniques.

A. APF-Based Controller

The control gains for the APF-based controller (20) were tuned by trial and error to $\mathbb{K}_p = \text{diag}(0.02, 0.02, 0.001)$, $\mathbb{K}_d = \text{diag}(0.04, 0.04, 0.002)$, $\alpha = 0.02$, $\gamma = (2\sigma_c^2)^{-1}$, and $\sigma_c = 1.5 \cdot 10^{-5}$ T. The angle of the error quaternion for this system is shown in Fig. 5.

Figure 5 shows that the pointing error of this mission can be kept under 3.5 deg, which does not satisfy the mission requirements. Moreover, the error bound of 3.5 deg is active throughout the lifetime of the mission when controller (20) is used, not only during singularities.

Regardless of how unnecessarily complicated controller (19) is, it has also been implemented in one of the simulations to assure that the omitted terms were not the reasons why the pointing error exceeded its allowable limit, however, revisiting the omitted terms did not improve the pointing accuracy at all.

B. APF-Based Controller with Singularity Prediction

The algorithm in Fig. 4 is tested by numerical simulations and a typical pointing performance of this technique is presented in Fig. 6. The singularity threshold is estimated empirically for the mission in Sec. III.C to be $B_{\text{th}} = 0.9$, whereas the prediction horizon is tuned by

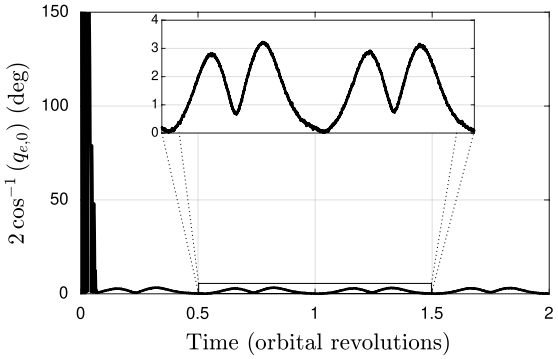

Fig. 5 Performance of the APF-based controller.

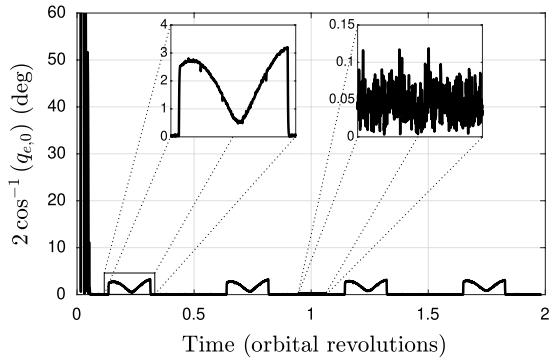

Fig. 6 Performance of the singularity prediction algorithm.

trial and error to $n = 100$ s. The controllers' parameters are tuned to $\mathbb{K}_p|_{\text{QF}} = \mathbb{K}_p|_{\text{APF}} = \text{diag}(0.02, 0.02, 0.001)$, $\mathbb{K}_d|_{\text{QF}} = \mathbb{K}_d|_{\text{APF}} = \text{diag}(0.04, 0.04, 0.002)$, $\alpha = 0.02$, $\gamma = (2\sigma_c^2)^{-1}$, and $\sigma_c = 1.5 \cdot 10^{-5}$ T.

The performance of this singularity avoidance technique is obviously better than of solely using the APF-based controller, because the pointing accuracy degrades only during singularities, not all the time as in Fig. 5.

C. Optimized RW Configuration

The optimization problem (22) has been solved for a near-polar orbit with an inclination of 87 deg over all the possible combinations of u and Ω^f, and the following results were obtained:

$$\left.\begin{aligned}\phi &= 40 \text{ deg}\\ \theta &= 28 \text{ deg}\\ \psi &= -64 \text{ deg}\end{aligned}\right\}, \qquad \text{rotation order is XYZ} \tag{23}$$

Figure 7 shows the maximum projection of $\hat{\boldsymbol{B}}^o$ ($\hat{\boldsymbol{B}}^o \equiv \hat{\boldsymbol{B}}^b$ for the case study of the paper) on any of the RW axes against all the possible combinations of u and Ω^f, assuming that the RW module is rotated by the optimized set of angles (23). It also shows the surface of the singularity threshold that has been identified for the case study, $B_{\text{th}} = 0.9$.

It is clear that after adopting the optimized RW configuration, the maximum projection of $\hat{\boldsymbol{B}}^o$ does not exceed the threshold except in three regions, the largest of which lasts for less than 9 deg in terms of u. The quaternion feedback controller is shown to not only work fine across singular points for longer periods of time, but also meet the mission requirements with a quality pointing accuracy (refer to cases X and Y in Fig. 1).

In practice, it may be found difficult to install the RW assembly with the optimized configuration for small CubeSats because of the size limitations. That is when the algorithmic singularity avoidance techniques come in handy. For spacecraft that are limited in size but still can allow for rotation of the RW assembly in certain directions, the module can be installed in a suboptimal orientation that results

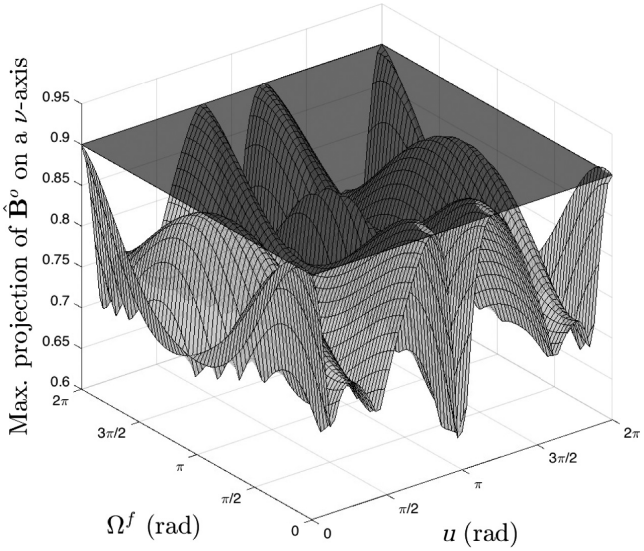

Fig. 7 Performance of the optimized RW arrangement.

from introducing more constraints to the optimization problem (22), $\theta = \psi = 0$, for example. This suboptimal configuration shall reduce the time over which the system is singular and hence reduce the time over which the pointing accuracy is compromised.

There are a couple of new prospects introduced by the proposed hardware solution, as it allows generalizing the proposed approaches for any nadir-pointing mission in any orbit. It can be easily seen in the example of an equatorial orbit. Obviously, for the initial RW layout (i.e., aligning three RWs with the principal moment of inertia axes), losing the wheel in the y direction makes the orbit highly singular (i.e., all points of the orbit are singular). However, changing the layout of the RWs at the design phase turns this situation to be completely void of singularities. The optimization problem (22) has been solved for a nadir-pointing mission for 10 different circular orbits at an altitude of 450 km with various orbital inclinations. The optimization is essentially run to determine the optimized configuration of RWs if the spacecraft is to be inserted in either of these orbits. Table 3 presents the maximum arc measure that contains successive singular points against the orbital inclination for the two cases of using the optimized and the initial configurations. The maximum singular arc measure ($u_{\max}$) in Table 3 is estimated by running the magnetic field model along the orbit that is signalized by the critical right ascension of the ascending node (RAAN), and measure the longest arc length. The critical RAAN is assumed to coincide with Ω^f for which the singular arc measure is the longest, which can be easily identified from surface plots like the one in Fig. 7.

In the case of failure of any one of the three available RWs, Table 3 suggests that simply positioning the RWs in the optimized arrangement can have a great impact in avoiding singularities. In some orbits, singularities can be completely avoided (e.g., orbits with inclinations 0, 10, 20, and 40 deg), whereas in some other orbits, singularities might be handled without the need to implement any singularity

Table 3 Singular portions of different orbits

	Maximum singular arc measure [deg]	
Inclination [deg]	Initial configuration	Optimized configuration
0	360	0
10	360	0
20	360	55.4
30	53.3	53.3
40	36.4	0
50	66.2	17.2
60	77.9	36.8
70	82.8	27.6
80	87.3	41.2
90	88.5	0

avoidance algorithms as the maximum singular arc measure is as low as of case X, which was handled quite well using only the quaternion feedback controller (4) (e.g., orbits with inclinations 50, 70, and 90 deg). In general, the probability of the spacecraft facing singularities can be lessened by changing the orientation of the RW assembly; however, this probability can still be high, which will require the usage of the algorithmic singularity avoidance techniques.

Note that only direct orbits are presented in Table 3; however, by virtue of symmetry, satellites in retrograde orbits ($\epsilon_r = \pi - \epsilon$, where ϵ_r is the inclination of the retrograde orbit, and ϵ is the inclination of the direct orbit) will experience the same singularity effect.

VI. Conclusions

This paper has developed fault-tolerant attitude control algorithms for a spacecraft that originally has three MTQs and three reaction wheels, but then any one of the reaction wheels experiences complete failure. Replacing the need for a redundant reaction wheel by enhancing the fault tolerance through a software solution can enable critical mass, volume, and power savings. In addition, such algorithms can be useful in systems with four reaction wheels that experience two reaction wheel failures. It is shown that the main challenge when using MTQs and two reaction wheels for three-axis attitude control is avoiding singular points in the control allocation, which are points along the orbit where it is physically impossible to realize the required control torque due to the physical limitations of MTQs. It is established that encountering singularities can eventually lead to a complete loss of control authority.

Software solutions are presented that can be used to avoid the singular regions. The two algorithmic techniques are shown by numerical experiments to effectively overcome the singularity problem, although at the expense of a slight degradation of pointing accuracy in the vicinity of near-singular zones. Nevertheless, control authority is maintained throughout the entire mission. The algorithms are based on prediction methods to determine when a singular point is close by, and on APFs classically used in obstacle avoidance algorithms. In addition, it is shown that the time spent close to the vicinity of singular regions can be reduced during the mission by designing the reaction wheels configuration in a particular way. A routine to optimize the reaction wheel configuration is presented, which minimizes the number and duration of encounters with singularities, and therefore reduces the probability of losing the control authority. Furthermore, this design strategy enhances the effectiveness of the software solutions.

The presented singularity avoidance techniques reduce the risk of mission failure when using only three reaction wheels in Earth orbiting missions. This is particularly relevant to CubeSat missions, where mass and volume are more critical. The proposed solutions provide an alternative approach to dealing with reaction wheel failure without the need for hardware redundancy.

Appendix A: Quaternions Fundamental Relations

In this paper, vector transformation from one reference frame to another is described by unit quaternions. A unit quaternion $\mathfrak{q} = [\, q_0 \quad \boldsymbol{q} \,]^T$ satisfies the relation $\boldsymbol{q}^T\boldsymbol{q} + q_0^2 = 1$. By saying that the unit quaternion $\mathfrak{q}^{yx} = [\, q_0 \quad \boldsymbol{q} \,]^T$ describes such transformations from the $\mathcal{F}^x$ frame to the $\mathcal{F}^y$ frame, it is implied that representations of any given vector $\boldsymbol{r}$ in these frames are related by

$$\boldsymbol{r}^y = \mathfrak{q}^{yx} \circ \boldsymbol{r}^x \circ \tilde{\mathfrak{q}}^{yx} \tag{A1}$$

where $\circ$ denotes the quaternion multiplication operator and $\tilde{\mathfrak{q}}^{yx} = \mathfrak{q}^{xy} = [\, q_0 \quad -\boldsymbol{q} \,]^T$ is the quaternion conjugate of $\mathfrak{q}^{yx}$.

The quaternion multiplication operation for the two quaternions $\mathfrak{q} = [\, q_0 \quad \boldsymbol{q} \,]^T$ and $\mathfrak{p} = [\, p_0 \quad \boldsymbol{p} \,]^T$ is performed as follows:

$$\mathfrak{q} \circ \mathfrak{p} = \begin{bmatrix} q_0 p_0 - \langle \boldsymbol{q}, \boldsymbol{p} \rangle \\ q_0 \boldsymbol{p} + p_0 \boldsymbol{q} + \boldsymbol{q} \times \boldsymbol{p} \end{bmatrix} \tag{A2}$$

A 3D vector is considered to be a quaternion with a zero scalar part.

By virtue of Eq. (A2), the following property can be proven for any two unit quaternions $\mathfrak{q}$ and $\mathfrak{p}$,

$$\widetilde{(\mathfrak{q} \circ \mathfrak{p})} = \tilde{\mathfrak{p}} \circ \tilde{\mathfrak{q}} \tag{A3}$$

Appendix B: Extension of the Mathematical Model

A. Environmental Model

A spacecraft in a low Earth orbit experiences disturbance torques that depend on the properties of the satellite such as its shape and the optical properties of its outer surfaces. Four disturbance torques were taken into account in all the simulations, gravity gradient, aerodynamic drag, solar radiation pressure, and residual magnetization torques.

The gravity gradient, aerodynamic drag, and solar radiation pressure torques were modeled according to the models presented in [20]. The residual magnetization torque is often found the most significant environmental torque for CubeSats, as they are small in size and have small moments of inertia [21]. This torque is modeled as follows:

$$\begin{aligned} \boldsymbol{m}^b_{\text{res}} &= \boldsymbol{m}^b_{\text{cnst}} + \boldsymbol{m}_{\text{rnd}}, \\ \boldsymbol{d}^b_{\text{res}} &= \boldsymbol{m}^b_{\text{res}} \times \boldsymbol{B}^b \end{aligned} \tag{B1}$$

where $\boldsymbol{m}^b_{\text{cnst}}$ is an arbitrary constant magnetic dipole vector, $\boldsymbol{m}_{\text{rnd}}$ is a uniformly distributed random vector, and $\boldsymbol{B}^b$ is the local geomagnetic field vector. The magnitude of $\boldsymbol{m}^b_{\text{cnst}}$ is set to $8 \cdot 10^{-3}$ A $\cdot$ m^2, which is almost the upper bound for $\|\boldsymbol{m}^b_{\text{res}}\|$ ($\|\boldsymbol{m}^b_{\text{res}}\| \leq 0.01$ for a 3U CubeSat [21]), while $\|\boldsymbol{m}_{\text{rnd}}\| = 0.1\|\boldsymbol{m}^b_{\text{cnst}}\|$.

B. Actuators' Models

1. Reaction Wheels Model

In this section, a model for mapping ideal control command to RW parameters is presented. The model of reaction wheels is augmented by two sources of noise, jitter and installation misalignment. Although reaction wheels experience friction torques, those are compensated for by an inner loop within the RW itself; that is why the friction effects are not accounted for in this paper.

Assuming that the attitude of the spacecraft is controlled solely by a combination of three or more reaction wheels arranged in a general configuration described by the configuration matrix $\mathbb{A}^b_w$, Eq. (1) can be rewritten as

$$\mathbb{J}^b \dot{\boldsymbol{\omega}}^b = -\boldsymbol{\omega}^b \times (\mathbb{J}^b \boldsymbol{\omega}^b + \mathbb{A}^b_w \boldsymbol{h}_w) \underbrace{- \mathbb{A}^b_w \dot{\boldsymbol{h}}_w}_{\boldsymbol{M}^b_{\text{ctrl}}} + \boldsymbol{d}^b_{\text{tot}} \tag{B2}$$

which yields

$$\begin{aligned} \dot{\boldsymbol{h}}_w &= -(\mathbb{A}^b_w)^\dagger \boldsymbol{M}^b_{\text{ctrl}}, \\ \dot{\boldsymbol{h}}_w &\coloneqq \text{Sat}(\dot{\boldsymbol{h}}_w, \dot{h}_{\max}), \\ \boldsymbol{h}_w &\coloneqq \text{Sat}(\boldsymbol{h}_w, h_{\max}), \\ \boldsymbol{M}^b_{\text{rw}} &= -\boldsymbol{\omega}^b \times \mathbb{A}^b_w \boldsymbol{h}_w - \mathbb{A}^b_w \dot{\boldsymbol{h}}_w \end{aligned} \tag{B3}$$

where $\boldsymbol{M}^b_{\text{rw}}$ is the actual torque generated by the RW module, $\boldsymbol{h}_w$ is an $n \times 1$ vector that contains the angular momentum each of the n reaction wheels has, $\mathbb{A}^b_w$ is a $3 \times n$ configuration matrix that contains the unit angular momentum vector of each of the n wheels as its columns in the $\mathcal{F}^b$ frame, and $(\mathbb{A}^b_w)^\dagger$ is the left pseudo-inverse of the matrix $\mathbb{A}^b_w$:

$$(\mathbb{A}^b_w)^\dagger = [(\mathbb{A}^b_w)^T \mathbb{A}^b_w]^{-1} (\mathbb{A}^b_w)^T \tag{B4}$$

The function $\text{Sat}(\boldsymbol{v}, \alpha_v)$ saturates all the elements of $\boldsymbol{v} = [\, v_1 \quad v_2 \quad \dots \quad v_n \,]^T$ using the saturation limits $\pm\alpha_v$ according to the following logic:

$$\mathrm{Sat}(\boldsymbol{v}, \alpha_v) = \begin{cases} v_i = \alpha_v \mathrm{sign}(v_i) & |v_i| \geq \alpha_v \\ v_i = v_i & \text{Otherwise} \end{cases} \tag{B5}$$

Equation (B3) is a mapping from the ideal control torque $\boldsymbol{M}^b_{\text{ctrl}}$ to the actuator parameters that are subject to noises and constraints such as saturation.

There are disturbances that affect the performance of RWs because they contain moving parts or because of manufacturing and installation errors. In this section, RW jitter and installation misalignment are modeled.

a. RW Jitter Model

One of reaction wheels' disturbances, which is known to be of importance for missions that require fine pointing [22], is jitter. In [22,23], two similar detailed wheel disturbance models are presented, with an algorithm to extract model parameters from a reaction wheel assembly microvibration test in [23]. A simplified model was developed in [24] under the assumption that the spacecraft is a perfect rigid body with no normal vibrational modes. In this paper, this model is generalized for any configuration of reaction wheels and is adopted in the simulations.

Jitter is generally caused by the static and dynamic imbalances in a reaction wheel. Static imbalances are radial asymmetries in the mass distribution of the reaction wheel, whereas dynamic imbalances are asymmetries in the mass distribution across the thickness of the wheel.

1) Effect of static imbalances

A wheel with static imbalances will make the spacecraft experience a periodic force with a constant magnitude that does not necessarily act through the center of mass of the spacecraft, which in turn generates torque.

For the sake of generalizing the model, one reaction wheel in the module will be dealt with at a time. If the RW has its local z axis aligned with the spin axis, with arbitrary x and y axes, the effect of static imbalance can be modeled by the following equations:

$$\boldsymbol{f}^b_{s,i} = S_i \Omega_i^2 \mathbb{R}_i \begin{bmatrix} \cos(\Omega_i t + \phi_i) \\ \sin(\Omega_i t + \phi_i) \\ 0 \end{bmatrix}, \qquad \mathbb{R}_i = [\,\hat{\boldsymbol{x}}^b_i \quad \hat{\boldsymbol{y}}^b_i \quad \hat{\boldsymbol{z}}^b_i\,] \tag{B6}$$

where $\boldsymbol{f}^b_{s,i}$ is the static imbalance induced force by the ith RW; S_i is the static imbalance in the ith wheel; Ω_i is the angular velocity of the ith wheel; $\hat{\boldsymbol{z}}^b_i$ is the direction of the spinning axis of the ith RW, namely, the ith column in the $\mathbb{A}^b_w$ matrix; and the two axes $\hat{\boldsymbol{x}}^b_i$ and $\hat{\boldsymbol{y}}^b_i$ are arbitrary. However, they complete the right-hand set $\hat{\boldsymbol{x}}^b_i \hat{\boldsymbol{y}}^b_i \hat{\boldsymbol{z}}^b_i$. ϕ_i is an arbitrary phase shift.

The static imbalance forces in each RW can be modeled by one equivalent force acting at the geometrical center of the corresponding reaction wheel. The total disturbance torque induced by static imbalances can be expressed as

$$\boldsymbol{d}^b_s = \sum_{i=1}^{n} \boldsymbol{r}^b_i \times \boldsymbol{f}^b_{s,i} \tag{B7}$$

where $\boldsymbol{r}^b_i$ is the location of the geometric center of the ith RW.

2) Effect of dynamic imbalances

A reaction wheel with dynamic imbalances will induce a periodic torque with a constant amplitude. This effect can be modeled as follows:

$$\boldsymbol{d}^b_{d,i} = D_i \Omega_i^2 \mathbb{R}_i \begin{bmatrix} \sin(\Omega_i t + \alpha_i) \\ -\cos(\Omega_i t + \alpha_i) \\ 0 \end{bmatrix} \tag{B8}$$

where D_i is the dynamic imbalance in the ith wheel.

The total disturbance torque induced by dynamic imbalances can be expressed as

$$\boldsymbol{d}^b_d = \sum_{i=1}^{n} \boldsymbol{d}^b_{d,i} \tag{B9}$$

The total jitter disturbance torque is the sum of the static and dynamic imbalances effects:

$$\boldsymbol{d}^b_{jit} = \boldsymbol{d}^b_s + \boldsymbol{d}^b_d \tag{B10}$$

b. RW Installation Misalignment Model

The problem of RW installation misalignment has been considered and compensated for in many studies in the literature (e.g., [25,26]). However, the adopted models for misalignment were developed for certain configurations and are not quite flexible to be applied to every configuration of reaction wheels.

In this paper, a simpler yet agile model for RWs misalignment is proposed. The output torque of the reaction wheel module is rotated by a misalignment quaternion as seen in the following relation:

$$\boldsymbol{M}^b_{\text{rw}} \coloneqq \mathfrak{q}_{\text{mis}} \circ \boldsymbol{M}^b_{\text{rw}} \circ \tilde{\mathfrak{q}}_{\text{mis}}, \qquad \tilde{\mathfrak{q}}_{\text{mis}} = [\cos(\theta_{\text{mis}}/2) \quad \sin(\theta_{\text{mis}}/2)\boldsymbol{e}_{\text{mis}}]^T \tag{B11}$$

where θ_{mis} is the error misalignment angle and $\boldsymbol{e}_{\text{mis}}$ is an arbitrary constant unit vector.

2. MTQ Model

MTQs generate torque by inducing a magnetic dipole that interacts with the Earth's magnetic field. The torque generated by a set of MTQs is described by the following general equation:

$$\boldsymbol{M}^b_{\text{mtq}} = \boldsymbol{m}^b \times \boldsymbol{B}^b \tag{B12}$$

where $\boldsymbol{m}^b$ is the magnetic moment vector generated by the MTQs and $\boldsymbol{B}^b$ is the local geomagnetic field vector at the satellite's position.

It is problematic to map the ideal control torque $\boldsymbol{M}^b_{\text{ctrl}}$ to the magnetic dipole vector if one is interested in controlling the torque in the three axes, as Eq. (B12) either does not have any solution for $\boldsymbol{m}^b$ (when $\boldsymbol{M}^b_{\text{mtq}}$ is NOT $\perp \boldsymbol{B}^b$) or has an infinite number of solutions for $\boldsymbol{m}^b$ (when $\boldsymbol{M}^b_{\text{mtq}}$ is $\perp \boldsymbol{B}^b$). It is easier, however, to map the ideal torque to MTQ dipole moment when one is interested in controlling the torque in one or two directions as discussed in Sec. III.B.

After mapping the ideal torque to the dipole moment of the MTQs, the dipole moment vector $\boldsymbol{m}^b$ can then be saturated and added to noise for a more realistic model (B13),

$$\boldsymbol{m}^b := \mathrm{Sat}(\boldsymbol{m}^b, m_{\max}) + \boldsymbol{m}_{\text{err}}, \qquad \boldsymbol{m}_{\text{err}} \sim \mathcal{N}_3(\boldsymbol{0}, \mathbb{S}_m) \tag{B13}$$

where $\mathbb{S}_m = \mathrm{diag}(\sigma_m^2, \sigma_m^2, \sigma_m^2)$ is the covariance matrix of the normally distributed error vector $\boldsymbol{m}_{\text{err}}$.

C. Determination Model

To have some sense of determination errors and their effect on controller performance, a simple model is presented, which introduces errors to the feedback states $\boldsymbol{\omega}^b$ and $\mathfrak{q}^{ib}$ as follows:

$$\boldsymbol{\omega}^b_{\text{det}} = \boldsymbol{\omega}^b + \boldsymbol{\omega}_{\text{err}}, \qquad \boldsymbol{\omega}_{\text{err}} \sim \mathcal{N}_3(\boldsymbol{0}, \mathbb{S}_\omega), \qquad \mathfrak{q}^{ib}_{\text{det}} = \mathfrak{q}^{\text{ib}} \circ \mathfrak{q}_{\text{err}} \tag{B14}$$

where $\mathbb{S}_\omega = \mathrm{diag}(\sigma_\omega^2, \sigma_\omega^2, \sigma_\omega^2)$ is the covariance matrix of the normally distributed error vector ω_{err} and the error unit quaternion $\mathfrak{q}_{\text{err}}$ is composed as follows:

$$\mathfrak{q}_{\text{err}} = [\cos(\theta_q/2) \quad \sin(\theta_q/2)\boldsymbol{e}_q]^T, \qquad \theta_q \sim \mathcal{N}_1(0, \sigma_q^2) \tag{B15}$$

where σ_q^2 is the variance of the normally distributed random angle θ_q, and $\boldsymbol{e}_q$ is a random unit vector.

Values for σ_q and $\mathbb{S}_\omega$ can be deduced from the literature in which various sensors and determination techniques have been used [17,27,28].

A simple model for the onboard magnetometers is presented here, as the magnetic field measurements are not only used within the attitude determination algorithms; they might also be required in the torque allocation (See Sec. III.B) and control algorithms (See Sec. IV). The measured geomagnetic field vector is modeled as the true local geomagnetic field vector (modeled by the IGRF12 model) with a normally distributed random error vector that has $\boldsymbol{\mu}_B = [\mu_B \quad \mu_B \quad \mu_B]$ as its mean vector and $\mathbb{S}_B = \text{diag}(\sigma_B^2, \sigma_B^2, \sigma_B^2)$ as its covariance matrix,

$$\boldsymbol{B}^b_{\text{meas}} = \boldsymbol{B}^b + \boldsymbol{B}_{\text{err}}, \qquad \boldsymbol{B}_{\text{err}} \sim \mathcal{N}_3(\boldsymbol{\mu}_B, \mathbb{S}_B) \tag{B16}$$

D. Inertia Uncertainty

Uncertainties in the moment of inertia matrix are accounted for in all of the simulations. The true inertia tensor $\mathbb{J}^b|_{\text{true}}$ is modeled as follows:

$$\mathbb{J}^b|_{\text{true}} = \mathbb{R}_J(\mathbb{J}^b|_{\text{est}} + \Delta\mathbb{J})\mathbb{R}_J^T \tag{B17}$$

where $\mathbb{J}^b|_{\text{est}} = \text{diag}(J_x, J_y, J_z)$ is the estimated inertia tensor, $\Delta\mathbb{J} = \text{diag}(\Delta J_x, \Delta J_y, \Delta J_z)$ is the uncertainty tensor, and $\mathbb{R}_J$ is an orthonormal rotation matrix, which can be calculated by converting the unit quaternion $\mathfrak{q}_J = [\cos(\theta_J/2) \quad \sin(\theta_J/2)\boldsymbol{e}_J]$ into a direction cosine matrix, where θ_J is small misalignment angle and $\boldsymbol{e}_J$ is an arbitrary unit vector.

Throughout the paper, and for simplicity, $\mathbb{J}^b$ is used to refer to either $\mathbb{J}^b|_{\text{true}}$ or $\mathbb{J}^b|_{\text{est}}$ depending on the place at which it is being used.

E. Kinematics of Error Signals

1. Kinematics of Error Quaternion

Recalling Eq. (5),

$$\mathfrak{q}_e = \tilde{\mathfrak{q}}_d \circ \mathfrak{q}^{ib} \tag{B18}$$

The time derivative of the error quaternion can be expressed as follows:

$$\dot{\mathfrak{q}}_e = \tilde{\mathfrak{q}}_d \circ \dot{\mathfrak{q}}^{ib} + \dot{\tilde{\mathfrak{q}}}_d \circ \mathfrak{q}^{ib} \tag{B19}$$

The desired quaternion must follow the kinematic equation (3), which yields

$$\dot{\mathfrak{q}}_d = \frac{1}{2}\mathfrak{q}_d \circ \boldsymbol{\omega}_d \tag{B20}$$

Applying the property (A3) to the kinematic equation (B20) yields

$$\dot{\tilde{\mathfrak{q}}}_d = \frac{1}{2} - \boldsymbol{\omega}_d \circ \tilde{\mathfrak{q}}_d \tag{B21}$$

Substituting from Eqs. (3) and (B21) into Eq. (B19), we get

$$\begin{aligned}\dot{\mathfrak{q}}_e &= \frac{1}{2}\tilde{\mathfrak{q}}_d \circ \mathfrak{q}^{ib} \circ \boldsymbol{\omega}^b - \frac{1}{2}\boldsymbol{\omega}_d \circ \tilde{\mathfrak{q}}_d \circ \mathfrak{q}^{ib} \\ &= \frac{1}{2}\mathfrak{q}_e \circ \boldsymbol{\omega}^b - \frac{1}{2}\boldsymbol{\omega}_d \circ \mathfrak{q}_e\end{aligned} \tag{B22}$$

It is obvious from Eq. (6) that the desired angular velocity can be expressed in the $\mathcal{F}^b$ frame as $\boldsymbol{\omega}_d^b = \tilde{\mathfrak{q}}_e \circ \boldsymbol{\omega}_d \circ \mathfrak{q}_e$, which can easily yield

$$\boldsymbol{\omega}_d = \mathfrak{q}_e \circ \boldsymbol{\omega}_d^b \circ \tilde{\mathfrak{q}}_e \tag{B23}$$

Substituting from Eq. (B23) into Eq. (B22),

$$\begin{aligned}\dot{\mathfrak{q}}_e &= \frac{1}{2}\mathfrak{q}_e \circ \boldsymbol{\omega}^b - \frac{1}{2}\mathfrak{q}_e \circ \boldsymbol{\omega}_d^b \\ &= \frac{1}{2}\mathfrak{q}_e \circ \boldsymbol{\omega}_e\end{aligned} \tag{B24}$$

2. Kinematics of Error Angular Velocity

Recalling Eq. (6),

$$\boldsymbol{\omega}_e = \boldsymbol{\omega}^b - \tilde{\mathfrak{q}}_e \circ \boldsymbol{\omega}_d \circ \mathfrak{q}_e \tag{B25}$$

The time derivative of the error angular velocity can be expressed as follows:

$$\dot{\boldsymbol{\omega}}_e = \dot{\boldsymbol{\omega}}^b - \dot{\tilde{\mathfrak{q}}}_e \circ \boldsymbol{\omega}_d \circ \mathfrak{q}_e - \tilde{\mathfrak{q}}_e \circ \boldsymbol{\omega}_d \circ \dot{\mathfrak{q}}_e - \tilde{\mathfrak{q}}_e \circ \dot{\boldsymbol{\omega}}_d \circ \mathfrak{q}_e \tag{B26}$$

Making use of Eq. (B24) and property (A3), Eq. (B26) can be rewritten as

$$\begin{aligned}\dot{\boldsymbol{\omega}}_e &= \dot{\boldsymbol{\omega}}^b + \frac{1}{2}\boldsymbol{\omega}_e \circ \tilde{\mathfrak{q}}_e \circ \boldsymbol{\omega}_d \circ \mathfrak{q}_e - \frac{1}{2}\tilde{\mathfrak{q}}_e \circ \boldsymbol{\omega}_d \circ \mathfrak{q}_e \circ \boldsymbol{\omega}_e - \tilde{\mathfrak{q}}_e \circ \dot{\boldsymbol{\omega}}_d \circ \mathfrak{q}_e \\ &= \dot{\boldsymbol{\omega}}^b + \boldsymbol{\omega}_e \times (\tilde{\mathfrak{q}}_e \circ \boldsymbol{\omega}_d \circ \mathfrak{q}_e) - \tilde{\mathfrak{q}}_e \circ \dot{\boldsymbol{\omega}}_d \circ \mathfrak{q}_e\end{aligned} \tag{B27}$$

Substituting for the value of $\dot{\boldsymbol{\omega}}^b$ from Eq. (B2), and assuming that the disturbances are perfectly compensated by $\boldsymbol{M}_{\text{ctrl}}$ (using disturbance rejection techniques), Eq. (B27) takes the following form:

$$\begin{aligned}\dot{\boldsymbol{\omega}}_e = {} & (\mathbb{J}^b)^{-1}[-\boldsymbol{\omega}^b \times (\mathbb{J}^b\boldsymbol{\omega}^b + \mathbb{A}_w^b\boldsymbol{h}_w) + \boldsymbol{M}_{\text{ctrl}}^b] \\ & + \boldsymbol{\omega}_e \times (\tilde{\mathfrak{q}}_e \circ \boldsymbol{\omega}_d \circ \mathfrak{q}_e) - \tilde{\mathfrak{q}}_e \circ \dot{\boldsymbol{\omega}}_d \circ \mathfrak{q}_e\end{aligned} \tag{B28}$$

Appendix C: B-Dot Expansion

Recalling Eq. (16),

$$\dot{\boldsymbol{B}}^b|_b = \dot{\boldsymbol{B}}^b|_i - \boldsymbol{\omega}^b \times \boldsymbol{B}^b \tag{C1}$$

where $\dot{\boldsymbol{v}}|_x$ denotes the rate of change of the vector $\boldsymbol{v}$ as seen by an observer attached to the $\mathcal{F}^x$ frame.

$\dot{\boldsymbol{B}}^b|_i$ can be expressed in terms of $\dot{\boldsymbol{B}}^o|_i$ as follows:

$$\dot{\boldsymbol{B}}^b|_i = \mathfrak{q}^{bo} \circ \dot{\boldsymbol{B}}^o|_i \circ \tilde{\mathfrak{q}}^{bo} \tag{C2}$$

For an Earth pointing mission, and when the satellite is close to the equilibrium point, $\mathfrak{q}^{bo} \approx [1 \quad 0 \quad 0 \quad 0]$, Eq. (C2) can be rewritten as

$$\dot{\boldsymbol{B}}^b|_i \approx \dot{\boldsymbol{B}}^o|_i \tag{C3}$$

Using the transport theorem to quantify $\dot{\boldsymbol{B}}^o|_i$ yields

$$\dot{\boldsymbol{B}}^o|_i = \dot{\boldsymbol{B}}^o|_o + [0 \quad \omega_0 \quad 0]^T \times \boldsymbol{B}^o \tag{C4}$$

The simplified direct dipole [16] can be used to model $\boldsymbol{B}^o$ as follows:

$$\boldsymbol{B}^o = B_0 \begin{bmatrix} \cos(u)\sin(\epsilon) \\ \cos(\epsilon) \\ -2\sin(u)\sin(\epsilon) \end{bmatrix} \tag{C5}$$

where $B_0 = \mu_e/\|\boldsymbol{r}\|$; $\mu_e = 7.812 \cdot 10^{15}$ T $\cdot$ m^3; $\boldsymbol{r}$ is the position vector of the spacecraft's center of mass, expressed in any reference frame; u is the argument of latitude at the satellite position; and ϵ is the inclination of the orbital plane.

Assuming constant B_0 and ϵ, and talking the time derivative for both sides of Eq. (C5) with $\dot{u} = \omega_0$ in mind, yields

$$\dot{\boldsymbol{B}}^o|_o = -\omega_0 B_0 \sin(\epsilon)\boldsymbol{l}, \qquad \boldsymbol{l} = \begin{bmatrix} \sin(u) \\ 0 \\ 2\cos(u) \end{bmatrix} \tag{C6}$$

Substituting from Eq. (C6) into Eq. (C4) yields

$$\dot{\boldsymbol{B}}^o|_i = -3\omega_0 B_0 \sin(\epsilon)\boldsymbol{l} \tag{C7}$$

Using the approximation (C3) and substituting in Eq. (C1), $\dot{\boldsymbol{B}}^b|_b$ can be written as

$$\begin{aligned} \dot{\boldsymbol{B}}^b|_b &\approx -3\omega_0 B_0 \sin(\epsilon)\boldsymbol{l} - \boldsymbol{\omega}^b \times \boldsymbol{B}^b \\ &\approx -3\omega_y B_0 \sin(\epsilon)\boldsymbol{l} - \boldsymbol{\omega}^b \times \boldsymbol{B}^b \end{aligned} \tag{C8}$$

In Eq. (C8), ω_0 is approximated to ω_y (the y component of the $\boldsymbol{\omega}^b$ vector). This is only true when the satellite is aimed to align its $\mathcal{F}^b$ frame with the $\mathcal{F}^o$ frame, and when it is close to its equilibrium point.

References

[1] Markley, F. L., and Crassidis, J. L., *Fundamentals of Spacecraft Attitude Determination and Control*, Vol. 33, Springer, 2014, Chap. 4.

[2] Li, J., Post, M., Wright, T., and Lee, R., "Design of Attitude Control Systems for CubeSat-Class Nanosatellite," *Journal of Control Science and Engineering*, Vol. 2013, Jan. 2013, pp. 1–15. https://doi.org/10.1155/2013/657182

[3] Lovera, M., and Astolfi, A., "Global Magnetic Attitude Control of Inertially Pointing Spacecraft," *Journal of Guidance, Control, and Dynamics*, Vol. 28, No. 5, 2005, pp. 1065–1072. https://doi.org/10.2514/1.11844

[4] Psiaki, M. L., "Nanosatellite Attitude Stabilization Using Passive Aerodynamics and Active Magnetic Torquing," *Journal of Guidance, Control, and Dynamics*, Vol. 27, No. 3, 2004, pp. 347–355. https://doi.org/10.2514/1.1993

[5] Dubos, G. F., Castet, J.-F., and Saleh, J. H., "Statistical Reliability Analysis of Satellites by Mass Category: Does Spacecraft Size Matter?" *Acta Astronautica*, Vol. 67, Nos. 5–6, 2010, pp. 584–595. https://doi.org/10.1016/j.actaastro.2010.04.017

[6] Zavoli, A., De Matteis, G., Giulietti, F., and Avanzini, G., "Single-Axis Pointing of an Underactuated Spacecraft Equipped with Two Reaction Wheels," *Journal of Guidance, Control, and Dynamics*, Vol. 40, No. 6, 2017, pp. 1465–1471. https://doi.org/10.2514/1.G002182

[7] Horri, N. M., and Palmer, P., "Practical Implementation of Attitude-Control Algorithms for an Underactuated Satellite," *Journal of Guidance, Control, and Dynamics*, Vol. 35, No. 1, 2012, pp. 40–45. https://doi.org/10.2514/1.54075

[8] Biggs, J. D., Bai, Y., and Henninger, H., "Attitude Guidance and Tracking for Spacecraft with Two Reaction Wheels," *International Journal of Control*, Vol. 91, No. 4, 2018, pp. 926–936. https://doi.org/10.1080/00207179.2017.1299944

[9] Forbes, J. R., and Damaren, C. J., "Geometric Approach to Spacecraft Attitude Control Using Magnetic and Mechanical Actuation," *Journal of Guidance, Control, and Dynamics*, Vol. 33, No. 2, 2010, pp. 590–595. https://doi.org/10.2514/1.46441

[10] Sakai, S.-I., Fukushima, Y., Saito, H., and Kaneda, R., "Studies on Magnetic Attitude Control System for the REIMEI Microsatellite," *AIAA Guidance, Navigation, and Control Conference and Exhibit*, AIAA Paper 2006-6450, 2006. https://doi.org/10.2514/6.2006-6450

[11] Roberts, B., Kruk, J., Ake, T., Englar, T., Class, B., and Rovner, D., "Three-Axis Attitude Control with Two Reaction Wheels and Magnetic Torquer Bars," *AIAA Guidance, Navigation, and Control Conference and Exhibit*, AIAA Paper 2004-5245, 2004. https://doi.org/10.2514/6.2004-5245

[12] Hur-Diaz, S., Wirzburger, J., and Smith, D., "Three Axis Control of the Hubble Space Telescope Using Two Reaction Wheels and Magnetic Torquer Bars for Science Observations," Advances in the Astronautical Sciences, Vol. 132, Univelt, Inc., 2008, pp. 335–350, https://www.scopus.com/inward/record.uri?eid=2-s2.0-62949229173partnerID=40 md5=60ec930240da17454cb535e34706b06e.

[13] Tudoroiu, N., and Khorasani, K., "Fault Detection and Diagnosis for Reaction Wheels of Satellite's Attitude Control System Using a Bank of Kalman Filters," *International Symposium on Signals, Circuits and Systems, 2005, ISSCS 2005*, Vol. 1, 2005, pp. 199–202. https://doi.org/10.1109/ISSCS.2005.1509888

[14] Baldi, P., Blanke, M., Castaldi, P., Mimmo, N., and Simani, S., "Adaptive FTC Based on Control Allocation and Fault Accommodation for Satellite Reaction Wheels," *2016 3rd Conference on Control and Fault-Tolerant Systems (SysTol)*, Inst. of Electrical and Electronics Engineers, New York, 2016, pp. 672–677. https://doi.org/10.1109/SYSTOL.2016.7739826

[15] Wie, B., Weiss, H., and Arapostathis, A., "Quaternion Feedback Regulator for Spacecraft Eigenaxis Rotations," *Journal of Guidance, Control, and Dynamics*, Vol. 12, No. 3, 1989, pp. 375–380. https://doi.org/10.2514/3.20418

[16] Ivanov, D., Ovchinnikov, M. Y., Penkov, V., Roldugin, D., Doronin, D., and Ovchinnikov, A., "Advanced Numerical Study of the Three-Axis Magnetic Attitude Control and Determination with Uncertainties," *Acta Astronautica*, Vol. 132, March 2017, pp. 103–110. https://doi.org/10.1016/j.actaastro.2016.11.045

[17] Mahfouz, A., Pritykin, D., Afanasev, A., Annenkova, A., and Latyshev, K., "Coordinated Attitude Determination and Control in a Swarm of CubeSats," *Proceedings of the International Astronautical Congress*, IAC, Oct. 2019, http://www.scopus.com/inward/record.url?eid=2-s2.0-85079153947&partnerID=MN8TOARS.

[18] Mclnnes, C. R., "Large Angle Slew Maneuvers with Autonomous Sun Vector Avoidance," *Journal of Guidance, Control, and Dynamics*, Vol. 17, No. 4, 1994, pp. 875–877. https://doi.org/10.2514/3.21283

[19] Mashtakov, Y., Ovchinnikov, M., Tkachev, S., and Shachkov, M., "Lyapunov Based Attitude Control Algorithm for Slew Maneuvers with Restrictions," Advances in the Astronautical Sciences, Vol. 163, Univelt, Inc., 2018, pp. 355–364, https://www.scopus.com/inward/record.uri?eid=2-s2.0-85049385374&partnerID=40 md5=50d569af5088989bb8ff7d20a848b4fa.

[20] Vallado, D. A., *Fundamentals of Astrodynamics and Applications*, 4th ed., Microcosm Press & Springer, 2013, Chap. 8.

[21] Annenkova, A., Afanasev, A., and Pritykin, D., "Revisiting the Residual Magnetization Problem in CubeSat Magnetic Attitude Control," *Advances in the Astronautical Sciences*, 2020 (to be published).

[22] Liu, K.-C., Maghami, P., and Blaurock, C., "Reaction Wheel Disturbance Modeling, Jitter Analysis, and Validation Tests for Solar Dynamics Observatory," *AIAA Guidance, Navigation and Control Conference and Exhibit*, AIAA Paper 2008-7232, 2008. https://doi.org/10.2514/6.2008-7232

[23] Masterson, R. A., Miller, D. W., and Grogan, R. L., "Development and Validation of Reaction Wheel Disturbance Models: Empirical Model," *Journal of Sound and Vibration*, Vol. 249, No. 3, 2002, pp. 575–598. https://doi.org/10.1006/jsvi.2001.3868

[24] Liu, L., "*Jitter and Basic Requirements of the Reaction Wheel Assembly in the Attitude Control System*," Massachusetts Inst. of Technology, Tech. Rept., Cambridge, MA, 2007.

[25] Zhang, A., Ni, J., and Karimi, H. R., "Reaction Wheel Installation Deviation Compensation for Overactuated Spacecraft with Finite-Time Attitude Control," *Mathematical Problems in Engineering*, Vol. 2013, 2013. https://doi.org/10.1155/2013/268904

[26] Hu, Q., Li, B., and Zhang, Y., "Robust Attitude Control Design for Spacecraft Under Assigned Velocity and Control Constraints," *ISA transactions*, Vol. 52, No. 4, 2013, pp. 480–493. https://doi.org/10.1016/j.isatra.2013.03.003

[27] Chagas, R. A. J., and Waldmann, J., "Rao-Blackwellized Particle Filter with Vector Observations for Satellite Three-Axis Attitude Estimation and Control in a Simulated Testbed," *SBA: Controle & Automação Sociedade Brasileira de Automatica*, Vol. 23, No. 3, 2012, pp. 277–293. https://doi.org/10.1590/S0103-17592012000300003

[28] Ni, S., and Zhang, C., "Attitude Determination of Nano Satellite Based on Gyroscope, Sun Sensor and Magnetometer," *Procedia Engineering*, Vol. 15, Jan. 2011, pp. 959–963. https://doi.org/10.1016/j.proeng.2011.08.177